Au@Cu₂O core@shell nanocrystals as dual-functional catalysts for sustainable environmental applications

Ming-Yu Kuo[a], Chih-Feng Hsiao[a], Yi-Hsuan Chiu[a], Ting-Hsuan Lai[a], Mei-Jing Fang[a], Jhen-Yang Wu[a], Jhih-Wei Chen[b], Chung-Lin Wu[b,c], Kung-Hwa Wei[a], Hsin-Chieh Lin[a,**], Yung-Jung Hsu[a,d,*]

[a] Department of Materials Science and Engineering, National Chiao Tung University, Hsinchu, 30010, Taiwan
[b] Department of Physics, National Cheng Kung University, Tainan, 70101, Taiwan
[c] National Synchrotron Radiation Research Center, Hsinchu, 30076, Taiwan
[d] Center for Emergent Functional Matter Science, National Chiao Tung University, Hsinchu, 30010, Taiwan

ABSTRACT

This work reports the synthesis of Au@Cu₂O core@shell nanocrystals with controllable shell thicknesses and demonstrates their use as the dual-functional catalyst that can continuously operate under illumination and darkness conditions for efficient *E. coli* inactivation. On account of the peroxidase mimics of the Au core and Fenton reactivity of the Cu₂O shell, the Au@Cu₂O nanocrystals exhibit intrinsic peroxidase-like property with the reaction kinetics in accordance with the typical Michaelis–Menten mechanism. On the other hand, time-resolved photoluminescence spectra suggest the prevalence of pronounced charge separation for Au@Cu₂O nanocrystals, an important advantage that is favourable for photocatalysis. By combining the photocatalytic capability with the peroxidase mimics features, Au@Cu₂O nanocrystals can perform practical photocatalytic decomposition of *E. coli* under visible light illumination but still show vital activity towards *E. coli* inactivation after light illumination was turned off. The current study delivers a new catalyst configuration by exploiting the multiple functionalities of nanosized Au and Cu₂O for advanced environmental and energy conversion applications.

1. Introduction

Increasing awareness of the need for sustainable chemistry has evoked interest to gear inorganic nanostructures to catalysis applications. In particular, Au nanocrystals have demonstrated distinct catalytic effects towards a variety of technologically important chemical reactions including low-temperature CO oxidation [1], reduction of nitro-aromatic compounds [2], and selective hydrogenations [3]. The use of Au nanocrystals as peroxidase mimics to catalyse the decomposition of H_2O_2 into ·OH radicals is especially appealing, owing to the importance of this reaction in both materials science and biological systems [4–6]. Compared to natural enzymes, Au nanocrystal-based artificial enzymes can endure much harsher environmental conditions such as extreme pH and high temperature [7]. Furthermore, Au nanocrystals as enzyme mimics are easier to prepare, purify, and store [8], providing high feasibility of further processing and usage. However, plain, unmodified Au nanocrystals are prone to aggregation during the

catalytic operations, hindering their further practical use [9]. As the talented motif of the two-component hybrid materials system, core@shell nanostructures in which Au nanocrystals are coated with a thin layer of shell materials have been proposed to tailor the catalytic properties of Au [10]. Since the Au core is protected by the shell materials from being aggregated during the reaction period, each of the Au particles can participate in the catalytic reactions, attaining a homogeneous reaction environment to facilitate the catalysis. Moreover, embedding of Au into the shell materials can alleviate the possible chemical corrosion of Au, extending the lifetime of the entire system and enabling long-term catalytic operation.

In addition to Au, metal oxide and metal sulphide nanostructures have also exhibited noticeable peroxidase-like activities [11–22]. Especially for transition metal oxides such as Cu_2O and Fe_3O_4, the Fenton-like chemistry of Cu^+ and Fe^{2+} can catalyse the generation of ·OH radicals in the presence of H_2O_2; thus, these oxides have been regarded as the robust peroxidase mimics for numerous environmental

and bioanalytical applications [11,12,17,18,23,24]. The combination of Au nanocrystals as the peroxidase mimics and Cu_2O nanostructures as the Fenton-like reagent is therefore desirable for the perceptive sketch of highly efficient artificial peroxidase enzymes. On the other hand, Cu_2O has featured prominently as a popular visible-light-driven photocatalyst owing to its moderate bandgap, favourable band structure, and high absorption coefficient. The incorporation of Au can further benefit Cu_2O for photocatalytic use because Au may function as charge separation enhancer to improve the overall carrier utilization [25–28]. To date, many hybrid materials systems composed of Cu_2O and Au have been shown effective in the relevant photocatalytic processes [29–41].

In this work, Au@Cu_2O core@shell nanocrystals have been demonstrated as a dual-functional catalyst that can continuously operate under illumination and in dark conditions for efficient *E. coli* inactivation. Note that previous studies on Au@Cu_2O hybrid nanocrystals mostly focused on the investigation of photocatalytic properties toward dye degradation [29–37], pollutant decomposition [38,39], as well as water splitting [40,41]. The use of such hybrid nanocrystals for bacterial inactivation has never been reported, not to mention the capability of continuous operation under illumination and darkness conditions. The preparation of Au@Cu_2O nanocrystals was achieved with the citrate-assisted chemical reduction method [42]. The peroxidase-like activity of Au@Cu_2O was evaluated with the typical Michaelis-Menten kinetics by using 3,3′,5,5′-tetramethylbenzidine (TMB) as the probe in the presence of H_2O_2. Owing to the peroxidase mimics of nano-sized Au and Fenton reactivity of Cu_2O, Au@Cu_2O can catalyse H_2O_2 decomposition to generate ·OH radicals for *E. coli* inactivation in a dark environment. On the other hand, because of the relative band alignment, introduction of Au can enhance the charge separation in Cu_2O under illumination, improving the photocatalytic activity for *E. coli* decomposition. By combining the photocatalytic capability with the peroxidase mimics features, Au@Cu_2O nanocrystals can perform practical photocatalytic decomposition of *E. coli* under visible light illumination but still show vital *E. coli* inactivation activity after light irradiation was switched off. This work delivers a new catalyst configuration by exploiting the multiple functionalities of nanosized Au and Cu_2O for advanced environmental and energy conversion applications.

2. Experimental section

2.1. Synthesis of Au@Cu_2O nanocrystals

A typical citrate reduction method was first used to prepare Au particles with the average diameter of 15 nm [43]. The deposition of Cu_2O on the Au particle surface was conducted using the chemical reduction method [42]. Briefly, 1.5 mL of NaOH solution (1.0 M) was added into 35 mL of deionized water, followed by the sequential addition of 1 mL of $CuSO_4$ (0.015, 0.02, 0.03, or 0.04 M), 3.0 mL of Au colloids (0.25 mM), and 0.5 mL of *L*-ascorbic acid (0.1 M). After stirred at 35 °C for 3 min, the reaction solution was centrifuged and washed several times with deionized water to collect the product. In this work, four different amounts of $CuSO_4$ (0.015, 0.02, 0.03, or 0.04 mmol) were used to prepare the Au@Cu_2O nanocrystals with increasing Cu_2O shell thicknesses. The thus-obtained samples were respectively denoted as Au@Cu_2O-1.5, Au@Cu_2O-2, Au@Cu_2O-3, and Au@Cu_2O-4.

2.2. Peroxidase-like activity measurements

To evaluate the peroxidase mimics activity, the samples were used as the artificial enzyme to conduct the catalytic oxidation of TMB in the presence of H_2O_2. Here, TMB is a chromogenic peroxidase probe, the oxidation of which generates a blue product (ox-TMB) that can be quantitatively characterized by measuring its absorbance at 652 nm. To perform the measurements, the catalyst suspension was first prepared by dispersing a specific amount of sample powder in 20 μL of ethanol,

followed by the mixing with 30 μL of H_2O_2 (10 M). The mixed solution was then added to the reaction solution containing 50 μL of TMB (15 mM) and 2.4 mL of acetic acid-sodium acetate buffer solution (0.1 M, pH = 4.0). Note that for pure Au and the four Au@Cu_2O nanocrystals, the same number of particles (approximately 1.85×10^{10}) were used for TMB oxidation in order to reveal the effect of Cu_2O shell thickness and highlight the beneficial feature of core@shell structures. The number of particles was determined by normalizing the concentration of Au based on the inductively coupled plasma mass spectrometry (ICP-MS) analytic results. The steady-state enzyme kinetics experiments were conducted by changing the concentration of H_2O_2 from 40 to 400 mM while fixing the concentration of TMB. By fitting to the Michaelis-Menten model, kinetics parameters such as K_M and v_{max} can be calculated to enable a global comparison among the different samples.

2.3. E. coli inactivation experiments

The *E. coli* cells were inoculated in a Luria-Bertani nutrient broth and incubated at 37 °C at 100 rpm for 20 h. Subsequently, the cells were harvested and centrifuged at 3500 rpm for 10 min, followed by discarding the supernatant and re-dispersing the cell pellet in phosphate-buffered saline (PBS) solution for conducting inactivation experiments. The bacteria levels were controlled by monitoring the optical density at 600 nm, approximately $10^8 \sim 10^9$ CFU/mL for different batches of experiments. The photocatalytic and dark-catalytic reactions were performed in a quartz cell. A 500 W Xe lamp coupled with a visible bandpass filter was used as the visible light illumination source for photocatalysis (300 mW/cm^2). To conduct inactivation experiments, 0.1 mg of nanocrystal powder was dispersed in 1.0 mL of PBS solution in the quartz cell, followed by the addition to 9 mL of the PBS solution containing *E. coli* cells. After that, the reaction solution was steadily stirred under visible light illumination to carry out photocatalytic *E. coli* inactivation. After 45 min of photocatalysis, light illumination was turned off and the *E. coli* inactivation was proceeded with the addition of H_2O_2 (294 μL, 0.1 M) under darkness condition. At certain time intervals, 200 μL aliquots of the reaction solutions were taken out and centrifuged to collect the precipitates. The precipitates were re-dispersed in 200 μL of PBS solution, poured onto the nutrient agar plates and then incubated at 37 °C for 20 h. The quantity of bacterial colony on each agar plate was counted and compared against the positive control.

2.4. Dye degradation experiments

Methyl orange (MO) was used as the test pollutant to examine the catalytic performance of the samples. To conduct photocatalytic MO degradation, 2.0 mg of the sample was dispersed in MO aqueous solution (10 mL, 1.0×10^{-5} M) in a quartz tube. After the adsorption-desorption equilibrium, the reaction solution was steadily stirred under light illumination (750 mW/cm^2). At certain time interval, 0.2 mL of the reaction solution was taken out and centrifuged to remove the catalyst powder. The absorbance at λ = 475 nm was then recorded to learn the concentration variation of the remaining MO. To perform peroxidase catalytic MO degradation, the reaction solution was prepared by dispersing 2.0 mg of the sample in MO aqueous solution (10 mL, 0.5×10^{-5} M) with the extra addition of H_2O_2 (0.3 mL, 30%), followed by steadily stirring under dark condition for 3 h.

2.5. Characterizations

Scanning electron microscopy (SEM) images were obtained using a Hitachi SU-8010 microscope. Transmission electron microscopy (TEM) images were taken on a JEOL JEM-F200 microscope. High-resolution TEM images, energy-dispersive X-ray spectroscopy (EDS) line-scan, and selected-area electron diffraction (SAED) patterns were acquired from JEOL JEM-3000 F. ICP-MS data were recorded on an Agilent 7500ce

spectrometer. X-ray diffraction (XRD) patterns were received using a Bruker D2 PHASER diffractometer. UV–vis absorption spectra were recorded on a Hitachi U-3900H spectrometer. To obtain steady-state photoluminescence (PL) spectra, a Hitachi F-4500 fluorescence spectrometer was employed. For time-resolved PL spectra, the data were collected in a customized single-photon counting system, in which a sub-nanosecond pulsed diode laser (λ_{ex} = 320 nm, PicoQuant, PLD 320) was installed and used as the excitation source. The ultraviolet photoelectron spectra (UPS) were acquired on a commercial "SPECs Phoibos 150 Analyzer" using 21.2 eV of Helium discharge as the excitation source. Measurements were performed by in-house chamber near "BL 09A1" of the National Synchrotron Radiation Research Center in Hsinchu, Taiwan.

3. Results and discussion

3.1. Structural investigations and optical properties

The growth of Cu_2O on the Au particles relied on the use of the citrate ligands remaining at the Au particle surface as binding reagent in the chemical reduction reaction [42]. Because of the citrate-Cu^{2+} linkage, the Cu_2O growth can occur entirely on the Au particle surface, producing Au@Cu_2O core@shell nanocrystals. As shown in Fig. 1, the core@shell feature for each of the resulting nanocrystals can be clearly identified from the obvious image contrast between the inner Au and outer Cu_2O regions. Importantly, pure Au particles and Au-free Cu_2O nanocrystals were seldom found in the product, assuring the integrity of the core@shell structures for conducting homogenous catalytic

reactions. By increasing the amount of the added Cu^{2+} precursor, the shell thickness of the grown Cu_2O increased accordingly, from 12.2 ± 1.7, 13.2 ± 1.8, 18.2 ± 2.2, to 20.8 ± 2.5 nm. The thus-obtained samples were respectively denoted as Au@Cu_2O-1.5, Au@Cu_2O-2, Au@Cu_2O-3, and Au@Cu_2O-4. According to the ICP-MS analytic results, the Cu_2O contents were determined to be 75.4, 79.8, 86.1 and 88.7 at%, respectively. Note that it was improbable to obtain Au@Cu_2O with thicker Cu_2O thickness than Au@Cu_2O-4 by using the current synthetic method. Further increasing the amount of Cu^{2+} precursor led to the separate growth of Cu_2O from Au particles. This outcome might be due to the prevalence of homogeneous nucleation of Cu_2O as a result of the relatively high supersaturation. On the other hand, pure Cu_2O nanocrystals which served as a counterpart sample for comparison purposes were also synthesized by using the same chemical reduction method without the addition of Au particles. As shown in Fig. S1 and S2 (supplementary data), pure Cu_2O shared similar microstructural features with Au@Cu_2O-4, displaying a rough surface with the typical diameter of approximately 59 nm. The detailed crystallographic structure of the samples was analysed by high-resolution TEM and XRD. In Fig. 2, the lattice-resolved image, EDS line-scan data and SAED pattern confirmed the core particles as fcc Au and the shell composition as cubic Cu_2O. The results of the XRD analysis shown in Fig. 3(a) further verified the high crystallinity for both the Au core and the grown Cu_2O shell. High crystallinity is essential for catalytic applications because charge carrier transfer can be facilitated. Fig. 3(b) further compares the UV–vis absorption spectra of the four Au@Cu_2O samples with those for pure Au particles and pure Cu_2O nanocrystals. The pure Au was characterized by a prominent surface plasmon

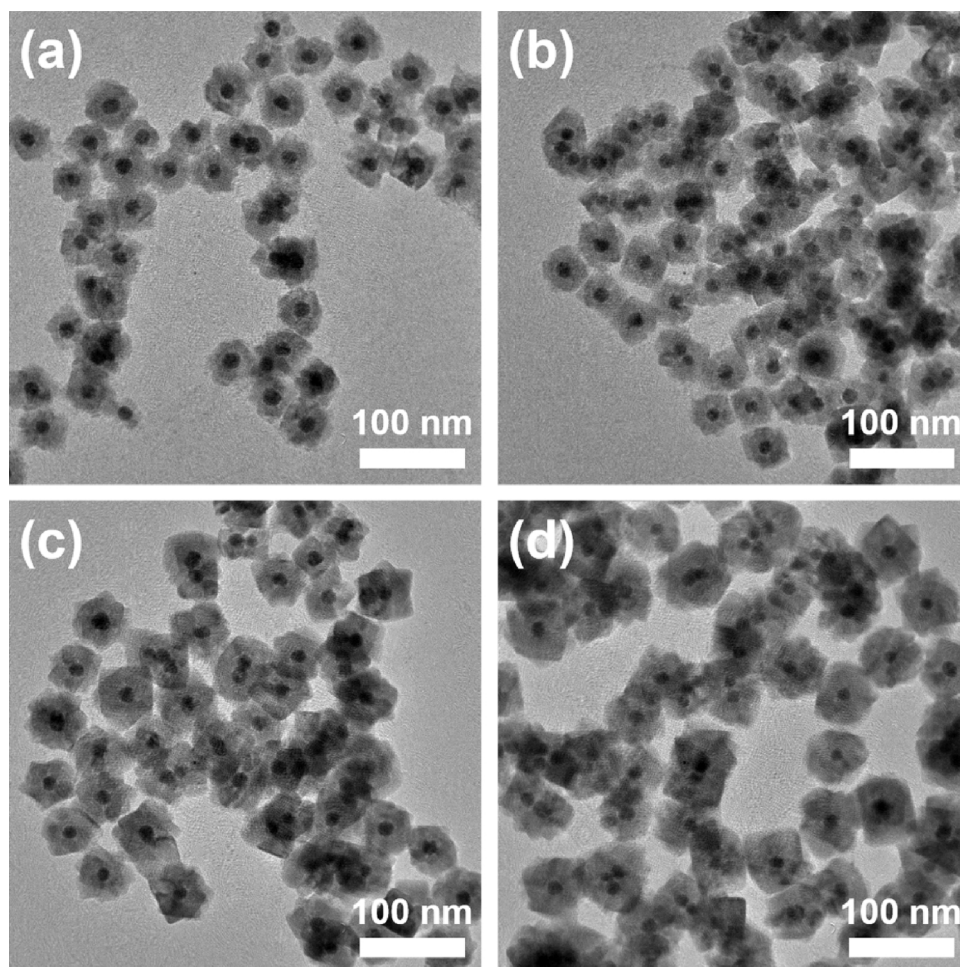**Fig. 1.** TEM images of (a) Au@Cu_2O-1.5, (b) Au@Cu_2O-2, (c) Au@Cu_2O-3, and (d) Au@Cu_2O-4.
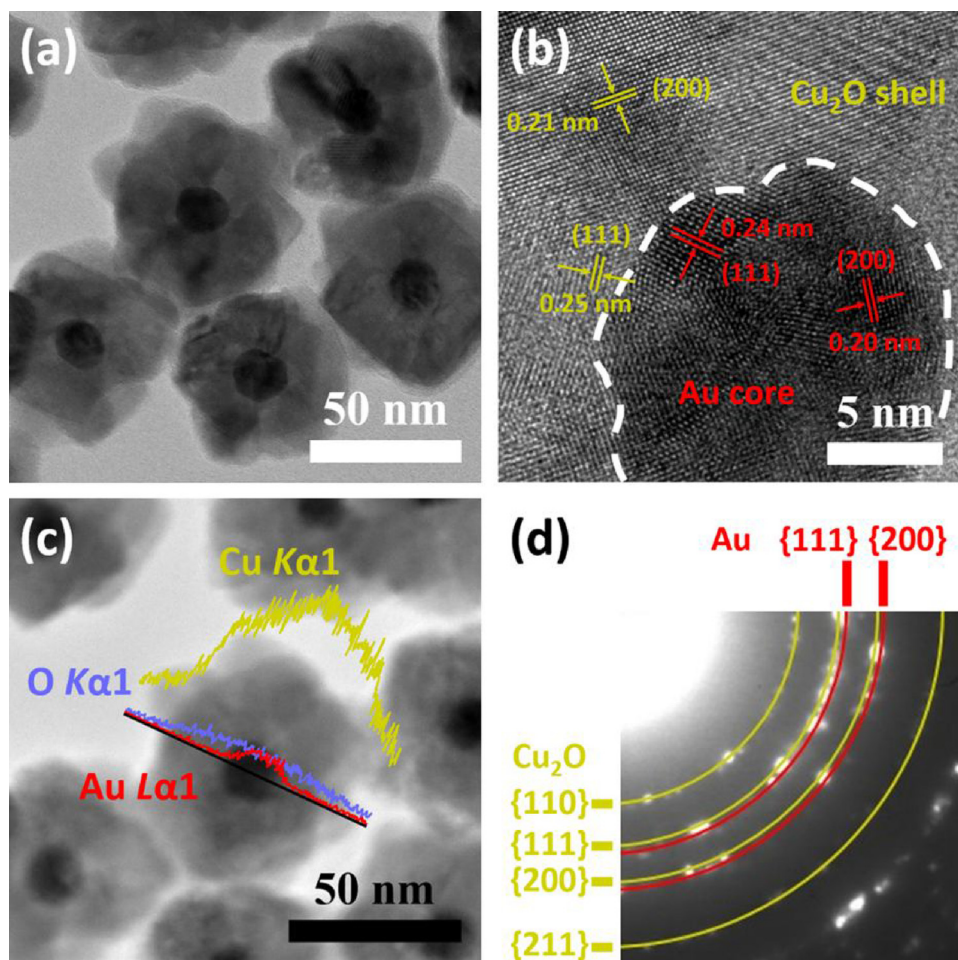
Fig. 2. (a) TEM image, (b) high-resolution TEM image, (c) EDS line-scan data, and (d) SAED pattern of Au@Cu$_2$O-4.
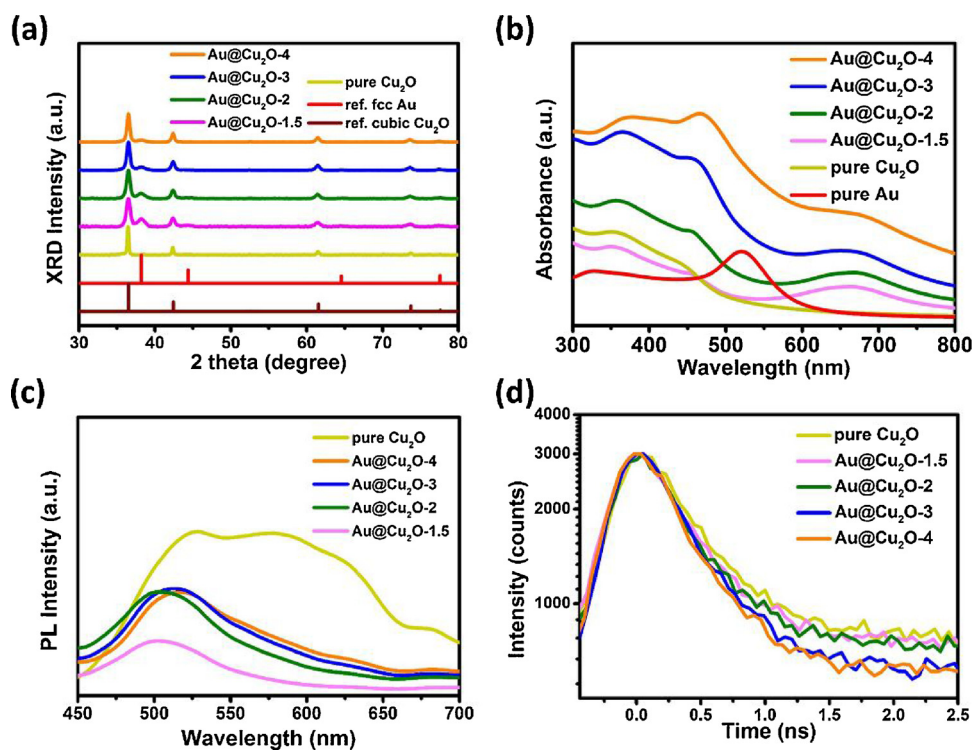

Fig. 3. (a) XRD patterns, (b) UV–vis absorption spectra, (c) steady-state PL spectra and (d) time-resolved PL spectra for pure Cu$_2$O and four Au@Cu$_2$O nanocrystals. In (a), standard patterns of fcc Au (JCPDS #65-2870) and cubic Cu$_2$O (JCPDS #77-0199) are included for reference. In (b), the result for pure Au particles is also included.

resonance (SPR) absorption peak at 520 nm, consistent with the reported value of Au colloids [2,4,5]. Comparatively, the SPR peak of the Au@Cu_2O nanocrystals largely shifted to the longer wavelength region, which was 667, 673, 674, and 682 nm for Au@Cu_2O-1.5, Au@Cu_2O-2, Au@Cu_2O-3, and Au@Cu_2O-4, respectively. The larger refractive index of the coated Cu_2O (n = 2.8–3.4 for Cu_2O) compared to that of the solvent (n = 1.33 for H_2O) may account for the observed red-shifted SPR for Au@Cu_2O [29,32,34,39]. Besides the SPR peak, an additional absorption edge with the onset at around 480 nm was also recorded for the four Au@Cu_2O nanocrystals. This absorption was ascribed to the bandgap absorption of Cu_2O [33,34,42], and can also be identified in the spectrum of the pure Cu_2O nanocrystals. The corresponding bandgap energy was determined to be 2.58 eV for both Au@Cu_2O and pure Cu_2O nanocrystals.

The optical properties of the samples were further investigated with PL spectroscopy. Fig. 3(c) displays the steady-state PL spectra of the five Cu_2O-based samples. Notably, a broad PL band associated with the excitonic band-to-band emission of Cu_2O was observed at 510 nm [40,44]. Compared to pure Cu_2O, the four Au@Cu_2O nanocrystals showed greatly reduced PL emissions, implying the prevalence of significant charge carrier separation. For Au@Cu_2O, the Au core may function as an electron acceptor for Cu_2O owing to the lower Fermi level of Au than that of Cu_2O [38,40]. The band alignment at the interface may induce electron transfer from Cu_2O to Au, prohibiting electron-hole recombination to enhance the overall charge separation. To examine the interfacial charge dynamics, time-resolved PL measurements were carried out. Fig. 3(d) compares the time-resolved PL spectra for the five Cu_2O-based samples. Relative to pure Cu_2O, the four Au@Cu_2O nanocrystals displayed faster PL decay kinetics, manifesting the occurrence of pronounced charge separation caused by the Au core. In order to quantitatively understand the charge transfer dynamics, these kinetics data were fitted using a biexponential decay model, from which an intensity-averaged carrier lifetime $< \tau >$ can be computed and compared. As noted in Table 1, the four Au@Cu_2O nanocrystals showed shorter carrier lifetimes than pure Cu_2O did, which was considered as the outcome of electron transfer from the Cu_2O shell to the Au core. Here, we assumed that the emission lifetime shortening of Au@Cu_2O was mostly caused by the interfacial charge transfer between Cu_2O and Au. The charge transfer rate constant (k_{ct}) can then be estimated as

$$k_{ct}(Cu_2O \rightarrow Au) = \frac{1}{<\tau>}(Au@Cu_2O) - \frac{1}{<\tau>}(Cu_2O) \quad [45\text{–}47].$$

For Au@Cu_2O-1.5, Au@Cu_2O-2, Au@Cu_2O-3, and Au@Cu_2O-4, the calculated k_{ct} values were respectively 0.58×10^8, 0.93×10^8, 4.60×10^8, and $5.58 \times 10^8 \, s^{-1}$. The obtained highest k_{ct} value for Au@Cu_2O-4 signified that charge carrier separation was much effective, giving rise to the promising potential use of Au@Cu_2O-4 as a highly efficient photocatalyst.

3.2. Peroxidase-like catalytic activity

To evaluate the peroxidase mimics behaviour, the samples were used as the artificial enzyme to conduct catalytic oxidation of TMB in the presence of H_2O_2. Note that TMB is a chromogenic peroxidase probe, which can be oxidized by ·OH radicals during the enzymatic

degradation of H_2O_2. The thus-formed oxidation product (ox-TMB) was blue, showing the absorption maximum at 652 nm [4,8,11–13,15–18,21,22,24]. Here, the oxidation of TMB was monitored by recording the absorbance of the blue-colour product at λ = 652 nm. Fig. 4(a) shows the time-dependent absorbance traces at 652 nm for the reaction solutions under different experimental conditions. A few significant points were noticed. First, the experiment without the catalyst addition showed negligible absorbance at 652 nm, suggesting that TMB oxidation did not occur in the absence of enzyme mimics. This outcome was essential for the validation of the intrinsic peroxidase property of the nanocrystal samples because the absorbance at 652 nm only increased in the presence of the nanocrystal samples. Second, pure Au particles exhibited fairly inferior peroxidase activity towards TMB oxidation. As derived from the citrate reduction process, pure Au particles were capped with citrate ligands and can be well-suspended in deionized water. Upon dispersed in an acetic acid buffer solution, these Au colloids were immediately agglomerated because of the disturbance of the surface electrostatic interactions. The structural aggregation may cause a decreased number of active sites to degrade the catalytic activity, which was accountable for the observed inactive feature of pure Au. Third, both pure Cu_2O and Au@Cu_2O were highly active for TMB oxidation, which can be attributed to the Fenton reactivity of the Cu species. The Cu^+ present at the Cu_2O surface may produce ·OH radicals from the Fenton reaction between Cu^+ and H_2O_2 [18,22], which oxidized TMB to show effective ox-TMB production. Much importantly, the four Au@Cu_2O nanocrystals showed superior peroxidase activity over pure Cu_2O. This observation reveals the augmented function of the Au core in promoting the peroxidase activity of Cu_2O. Since the core Au particles were protected by the Cu_2O shell from being aggregated during the catalytic reaction, each of the Au particles can participate in TMB oxidation to facilitate the overall catalysis. Last, the peroxidase activity of Au@Cu_2O increased with increasing shell thickness, with Au@Cu_2O-4 showing the highest efficiency. Note that the number of particles of the four Au@Cu_2O nanocrystals used for TMB oxidation was fixed at a constant value. Under this situation, Au@Cu_2O with larger shell thickness was expected to provide more accessible Cu_2O surface with a higher number of active sites. The Fenton reaction can therefore be boosted at the nanocrystal surface to produce more ·OH radicals for expediting TMB oxidation, which may account for the observed highest peroxidase activity of Au@Cu_2O-4.

To further analyse the peroxidase mechanism, the steady-state enzyme kinetics experiments were performed by changing the concentration of H_2O_2 substrate while fixing the concentration of the TMB probe [11,12,16,18,19]. Fig. 4(b) compares the apparent steady-state reaction velocities at different H_2O_2 concentrations for the five Cu_2O-based nanocrystal samples. Here, the apparent reaction velocities were obtained by calculating the slopes of the initial concentration of ox-TMB over reaction time. The concentration of ox-TMB was determined from the absorbance data by applying a known molar absorption coefficient of 39,000 $M^{-1} cm^{-1}$ [12,18]. All of the samples exhibited hyperbolic kinetics characteristic of a typical Michaelis-Menten mechanism. The Michaelis-Menten parameters can be further estimated from the Lineweaver–Burk plots shown in Fig. 4(c) according to $1/v = 1/v_{max} + K_M/v_{max}[S]$. Here, v and v_{max} respectively stand for the initial and maximum velocities, [S] represents the concentration of H_2O_2 substrate, and K_M denotes the Michaelis constant serving as an index to describe the affinity of the enzyme to the substrate. As summarized in Table 2, the five Cu_2O-based samples were found to show fairly close K_M values, suggesting their affinities to H_2O_2 substrate were nearly identical. On the other hand, the v_{max} value of Au@Cu_2O increased with increasing shell thickness, which was fundamentally consistent with the results presented in Fig. 4(a). For Au@Cu_2O-4, the obtained v_{max} was 1.4 times higher than that of pure Cu_2O, signifying that the protected Au core can substantially promote the peroxidase activity of Cu_2O. It should be noticed that the obtained K_M and v_{max} of Au@Cu_2O nanocrystals were comparable and even superior to those

Table 1
Fitted results of time-resolved PL spectra for pure Cu_2O and four Au@Cu_2O.

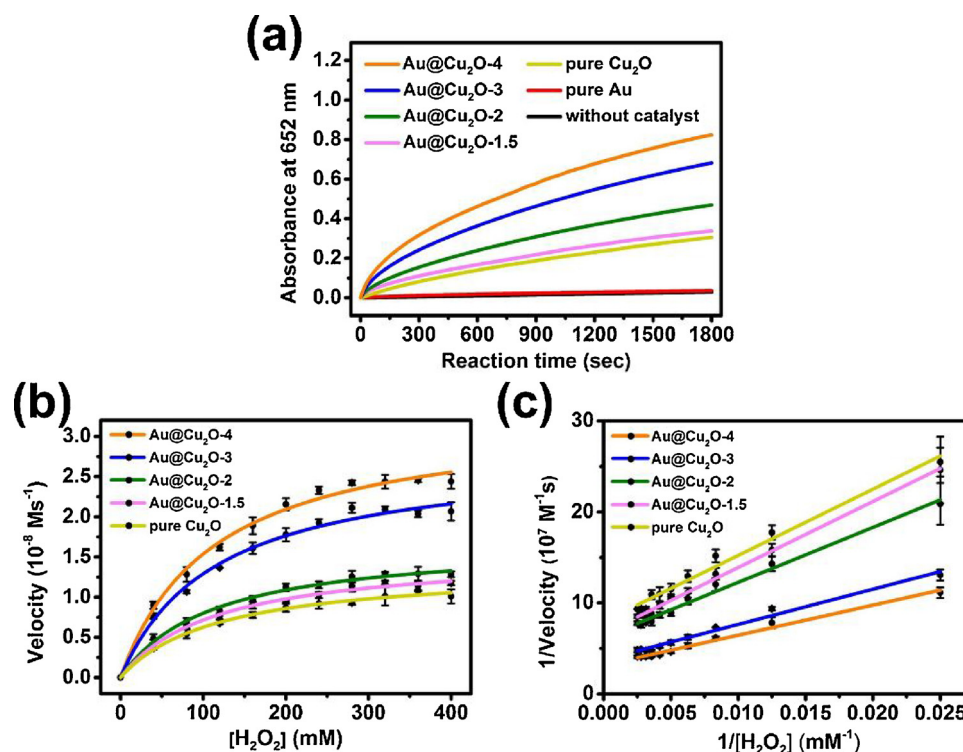| entry	A_1 (%)	τ_1 (ns)	A_2 (%)	τ_2 (ns)	$< \tau >$ (ns)	χ^2	k_{ct} ($\times 10^8 s^{-1}$)
pure Cu_2O	3.88	5.05	96.12	0.54	1.78	1.05	–
Au@Cu_2O-1.5	3.24	4.98	96.76	0.51	1.61	1.06	0.58
Au@Cu_2O-2	3.04	4.67	96.96	0.41	1.53	1.01	0.93
Au@Cu_2O-3	2.00	3.88	98.00	0.39	0.98	1.03	4.60
Au@Cu_2O-4	1.79	3.63	98.21	0.31	0.89	1.06	5.58

Fig. 4. (a) Time-dependent absorbance traces at 652 nm for TMB solutions catalysed by different samples. (b) Steady-state kinetics analysis of TMB oxidation on different samples. (c) Double reciprocal plots of reaction velocity with different H_2O_2 concentrations for different samples.

Table 2
Comparison of kinetics parameters over pure Cu_2O and four $Au@Cu_2O$.

entry	v_{max} ($\times 10^{-8}$ Ms^{-1})	K_M (mM)
pure Cu_2O	1.36	118.09
$Au@Cu_2O$-1.5	1.53	115.96
$Au@Cu_2O$-2	1.70	112.82
$Au@Cu_2O$-3	2.79	115.89
$Au@Cu_2O$-4	3.28	113.21

reported for promising peroxidase mimics, such as Fe_3O_4 and Co_3O_4 nanoparticles [11,15]. This outcome illustrates that the present $Au@Cu_2O$ nanocrystals may function as a new class of artificial peroxidase enzymes that holds great promise for catalytic applications.

3.3. Photocatalytic and peroxidase catalytic E. coli inactivation

In addition to peroxidase mimics, the $Au@Cu_2O$ nanocrystals also represented a versatile hybrid photocatalyst paradigm for realizing advanced photocatalytic utilizations [29–41]. By combining the photocatalytic capacity with the peroxidase mimics and Fenton reactivity, the present $Au@Cu_2O$ may find unique yet viable uses in intriguing catalytic processes. To demonstrate the versatility, $Au@Cu_2O$ nanocrystals were employed as the dual-functional catalyst for conducting sustainable *E. coli* inactivation under illumination and darkness conditions. Here, the *E. coli* inactivation experiments were designed to allow photocatalysis under illumination in the beginning, which was taken over by the subsequent execution of peroxidase catalysis in the dark environment. Fig. 5(a) depicts the experimental results by using the three representative samples as the catalyst, pure Au, pure Cu_2O and $Au@Cu_2O$-4. Under visible light illumination, both pure Cu_2O and $Au@Cu_2O$-4 exhibited vigorous activity towards *E. coli* inactivation, reflecting the inherent photocatalytic capacity of the Cu_2O component. On the other hand, pure Au was photocatalytically inactive as expected. Noticeably, $Au@Cu_2O$-4 achieved a 4-log reduction in viable *E. coli*

count within 45 min of irradiation, which was three orders of magnitude greater than the result obtained by pure Cu_2O at the same illumination time. The pronounced charge separation rendered by the electron transfer from Cu_2O to Au may account for the enhanced photocatalytic activity of $Au@Cu_2O$-4. After 45 min of photocatalytic reaction, light irradiation was turned off and the *E. coli* inactivation was subsequently operated with the addition of H_2O_2 in dark environment. Both pure Cu_2O and $Au@Cu_2O$-4 continued to show vital activity of *E. coli* inactivation after the light irradiation was switched off. Such a remarkable dark-catalytic effect can be connected to the peroxidase mimics function of Au and the Fenton reactivity of Cu_2O, which enabled the production of ·OH radicals in the dark to proceed with *E. coli* inactivation. Pure Au particles again were found inactive under darkness conditions, in agreement with the TMB oxidation results. As noted in Fig. 5(a), the catalytic effect of pure Cu_2O in the dark persisted for 75 min, attaining an additional 2-log decrease of *E. coli* concentration. In contrast, the use of $Au@Cu_2O$-4 during the same reaction period led to the complete inactivation for the remaining *E. coli* cells, eliminating *E. coli* populations by 5-log CFU/mL.

In order to determine the band structure of $Au@Cu_2O$, we further conducted UPS measurements on the constituent components. In Fig. S4 (supplementary data), the UPS spectra of pure Au and pure Cu_2O showed distinct secondary-electron cut-off energies, presenting a work function value of 4.59 and 4.33 eV, respectively. The UPS spectra at the valence band distribution region on the other hand disclosed the valence band level vs. Fermi level (E_F), which was respectively determined as 0 and 1.10 eV for Au and Cu_2O. By adding the work function value, the valence band level (E_{VB}) of Cu_2O was obtained as -5.43 eV vs. vacuum. Further adding the apparent bandgap (2.52 eV for Cu_2O as determined from Tauc plot) gave rise to the conduction band level (E_{CB}) of -2.91 eV vs. vacuum. On the basis of the UPS data, the band structure of $Au@Cu_2O$ can be delineated in Fig. 5(b). Under light illumination, the photoexcited electrons of Cu_2O would preferentially transfer to Au owing to the higher E_F of Cu_2O than the E_F of Au; meanwhile, abundant photogenerated holes were delocalized at Cu_2O
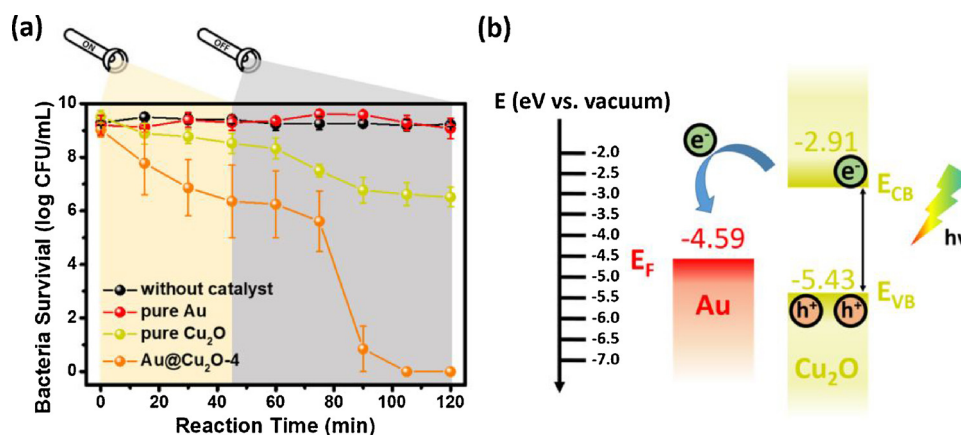
Fig. 5. (a) Results of sustainable *E. coli* inactivation under light illumination and darkness conditions by using different catalyst samples. (b) Proposed band structure and interfacial charge transfer process for Au@Cu$_2$O.
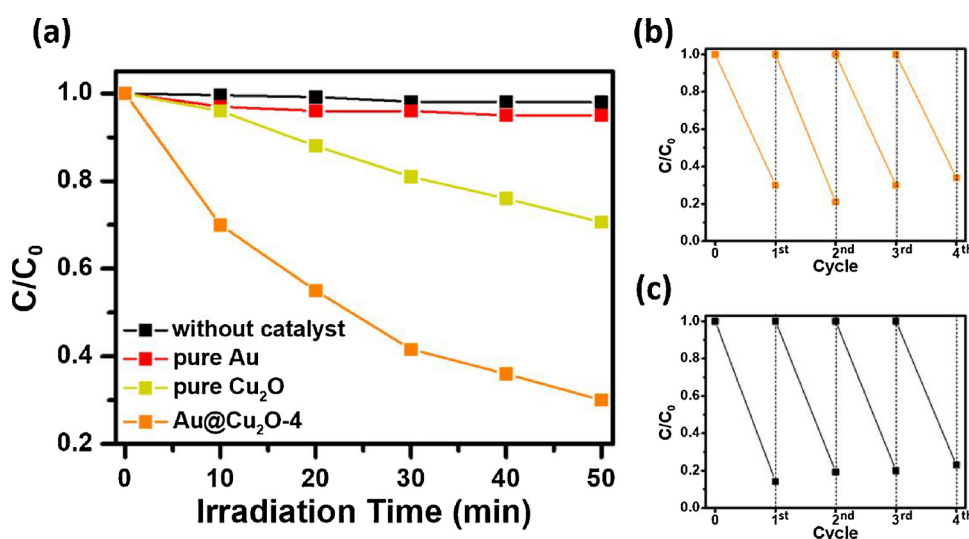

Fig. 6. (a) Comparative results of photocatalytic MO degradation by using pure Au, pure Cu$_2$O and Au@Cu$_2$O-4. (b) and (c) show the recycling tests of MO degradation on Au@Cu$_2$O-4 under photocatalytic and peroxidase catalytic conditions, respectively. Each cycle was conducted for 50 min for photocatalysis and 3 h for peroxidase catalysis.

to achieve effective charge separation. The results of steady-state and time-resolved PL spectra may support the proposed band structure.

A plausible mechanism was conceived to interpret the synergy of photocatalysis, peroxidase mimics and Fenton reactivity for Au@Cu$_2$O nanocrystals for continuous operation of *E. coli* inactivation under light illumination and darkness conditions. Under light illumination, abundant photogenerated holes were delocalized at the Cu$_2$O surface, which may directly oxidize *E. coli* cells to achieve cell inactivation [48]. The inactivation of *E. coli* can also be recognized from the cell structural damage as revealed by the microscopy analysis. As shown in Fig. S3(a) and S3(b) (supplementary data), upon the photocatalysis operation, the *E. coli* cell surface showed deadly alterations, appearing wrinkled and partly collapsed in the central region [49–51]. Under darkness conditions, both the peroxidase mimics of Au core and the Fenton reactivity of the Cu$_2$O shell induced the production of ·OH radicals. These reactive oxygen species may cause fatal damages to the cell structure, resulting in the death of *E. coli*. As Fig. S3(c) and S3(d) (supplementary data) reveal, the *E. coli* treated in the dark experienced a disruption of the cell membrane and even the leakage of cellular content, finally losing the viability as observed [52,53]. It is worth noting that the catalyst loading for *E. coli* inactivation experiments in the present work (10 mg/L) was much smaller than that used in other photocatalytic systems (approximately 100~1000 mg/L) [48–50,54,55]. The amount of H$_2$O$_2$ needed for carrying out *E. coli* inactivation in the dark (3 mM) was also lower than that employed in the Fenton-assisted cases (around 10–15 mM) [56,57]. This outcome further highlights the advantageous features of

the current Au@Cu$_2$O nanocrystals for environmental purification applications, especially in the cases when the chemical dose is important.

3.4. MO degradation and durability tests

The durability is another important attribute for evaluating the practicability of catalysts. Here, we evaluated the durability of Au@Cu$_2$O toward MO degradation, a typical example of pollutant removal [58–60]. Fig. 6(a) first compares the photocatalytic performance on relevant samples under visible light illumination. As expected, the Au@Cu$_2$O-4 exhibited superior photocatalytic activity of MO degradation over pure Cu$_2$O and pure Au. The durability tests were then carried out by conducting MO degradation under photocatalytic and peroxidase catalytic conditions. As shown in Fig. 6(b) and (c), the MO degradation performance of Au@Cu$_2$O was fairly stable upon four repeated usages under both photocatalytic and peroxidase catalytic conditions, ensuring their extended use for environmental purification.

4. Conclusion

In conclusion, Au@Cu$_2$O nanocrystals with controllable shell thicknesses were prepared and employed as peroxidase mimics to catalyse the generation of ·OH radicals in the presence of H$_2$O$_2$. Compared to pure Au and pure Cu$_2$O, the Au@Cu$_2$O nanocrystals exhibited substantially enhanced peroxidase activity as a result of the advantageous features of core@shell structures. The peroxidase activity of Au@Cu$_2$O

increased with increasing shell thickness, which is attributed to the enhanced Fenton kinetics rendered by the increased number of accessible Cu$_2$O surface sites. On the other hand, the function as electron acceptor of Au can promote overall charge separation for Cu$_2$O, giving rise to the promising potential of Au@Cu$_2$O for use as photocatalysts. By combining the photocatalytic capability with the peroxidase mimics features, Au@Cu$_2$O nanocrystals can carry out practical photocatalytic decomposition of *E. coli* under visible light illumination but still show vital activity towards *E. coli* inactivation after light illumination was turned off. The current Au@Cu$_2$O nanocrystals may continuously operate under light illumination and darkness conditions for sustainable *E. coli* inactivation, which is practically valuable for real-world environmental purification applications, especially when the sustaining operation is required. Our discovery represents a sophisticated yet practical strategy for the construction of new types of viable catalysts for environmental and energy conversion applications.

Acknowledgements

Appendix A. Supplementary data

Supplementary material related to this article can be found, in the online version, at doi:https://doi.org/10.1016/j.apcatb.2018.09.075.

References

[1] M. Haruta, T. Kobayashi, H. Sano, N. Yamada, Chem. Lett. 16 (1987) 405–408.
[2] R. Fenger, E. Fertitta, H. Kirmse, A.F. Thünemannc, K. Rademann, Phys. Chem. Chem. Phys. 14 (2012) 9343–9349.
[3] E. Bus, R. Prins, J.A. van Bokhoven, Catal. Commun. 8 (2007) 1397–1402.
[4] X. Chen, X. Tian, B. Su, Z. Huang, Xi Chenc, M. Oyamad, Dalton Trans. 43 (2014) 7449–7454.
[5] C.-W. Lien, C.-C. Huang, H.-T. Chang, Chem. Commun. 48 (2012) 7952–7954.
[6] W. Haider, A. Hayat, Y. Raza, A.A. Chaudhry, I.-U.- Rehmand, J.L. Marty, RSC Adv. 5 (2015) 24853–24858.
[7] K. Chattopadhyay, S. Mazumdar, Biochemistry 39 (2000) 263–270.
[8] H. Sun, X. Jiao, Y. Han, Z. Jiang, D. Chen, Eur. J. Inorg. Chem. 1 (2013) 109–114.
[9] J. Ge, Q. Zhang, T. Zhang, Y. Yin, Angew. Chem. Int. Ed. 47 (2008) 8924–8928.
[10] N. Zhang, S. Liu, Y.-J. Xu, Nanoscale 4 (2012) 2227–2238.
[11] L. Gao, J. Zhuang, L. Nie, J. Zhang, Y. Zhang, N. Gu, T. Wang, J. Feng, D. Yang, S. Perrett, X. Yan, Nat. Nanotechnol. 2 (2007) 577–583.
[12] A.K. Dutta, S.K. Maji, D.N. Srivastava, A. Mondal, P. Biswas, P. Paul, B. Adhikary, ACS Appl. Mater. Interfaces 4 (2012) 1919–1927.
[13] R. André, F. Natálio, M. Humanes, J. Leppin, K. Heinze, R. Wever, H.-C. Schröder, W.E.G. Müller, W. Tremel, Adv. Funct. Mater. 21 (2011) 501–509.
[14] X. Xiao, Q. Luan, X. Yao, K. Zhou, Biosens. Bioelectron. 24 (2009) 2447–2451.
[15] J. Mu, Y. Wang, M. Zhaob, L. Zhang, Chem. Commun. 48 (2012) 2540–2542.
[16] S. Kandula, P. Jeevanandam, RSC Adv. 5 (2015) 5295–5306.
[17] W. He, H. Jia, X. Li, Y. Lei, J. Li, H. Zhao, L. Mi, L. Zhangb, Z. Zheng, Nanoscale 4 (2012) 3501–3506.
[18] Y. Liu, G. Zhu, C. Bao, A. Yuan, X. Shenb, Chin. J. Chem. 32 (2014) 151–156.
[19] G.L. Li, P. Ma, Y.F. Zhang, X.L. Liu, H. Zhang, W.M. Xue, Y. Mi, Y.E. Luo, H.M. Fan, J. Mater. Sci. 51 (2016) 3979–3988.
[20] W. Luo, Y.-S. Li, J. Yuan, L. Zhu, Z. Liu, H. Tang, S. Liu, Talanta 81 (2010) 901–907.
[21] W. Shi, X. Zhang, S. He, Y. Huang, Chem. Commun. 47 (2011) 10785–10787.
[22] X.-F. Lu, X.-J. Bian, Z.-C. Li, D.-M. Chao, C. Wang, Sci. Rep. 3 (2013) 2955–2961.
[23] Z.-M. Cui, Z. Chen, C.-Y. Cao, L. Jiang, W.-G. Song, Chem. Commun. 49 (2013) 2332–2334.
[24] Q.W. Shu, C.M. Li, P.F. Gao, M.X. Gao, C.Z. Huang, RSC Adv. 5 (2015) 17458–17465.
[25] N.S. Han, D. Kim, J.W. Lee, J. Kim, H.S. Shim, Y. Lee, D. Lee, J.K. Song, ACS Appl. Mater. Interfaces 8 (2016) 1067–1072.
[26] Y.-C. Pu, W.-H. Lin, Y.-J. Hsu, Appl. Catal. B Environ. 163 (2015) 343–351.
[27] Y.-C. Pu, G. Wang, K.-D. Chang, Y. Ling, Y.-K. Lin, B.C. Fitzmorris, C.-M. Liu, X. Lu, Y. Tong, J.Z. Zhang, Y.-J. Hsu, Y. Li, Nano Lett. 13 (2013) 3817–3823.
[28] J.-M. Li, H.-Y. Cheng, Y.-H. Chiu, Y.-J. Hsu, Nanoscale 8 (2016) 15720–15729.
[29] B. Lu, A. Liu, H. Wu, Q. Shen, T. Zhao, J. Wang, Langmuir 32 (2016) 3085–3094.
[30] R. Chen, Juan Lu, Shengnan Liu, Min Zheng, Zuoshan Wang, J. Mater. Sci. 53 (2018) 1781–1790.
[31] D. Jiang, W. Zhou, X. Zhong, Y. Zhang, X. Li, ACS Appl. Mater. Interfaces 6 (2014) 10958–10962.
[32] Y. Wang, M. Zheng, S. Liu, Z. Wang, Nanoscale Res. Lett. 11 (2016) 390–397.
[33] G.-Z. Yuan, C.-F. Hsia, Z.-W. Lin, C. Chiang, Y.-W. Chiang, M.H. Huang, Chem. Eur. J. 22 (2016) 12548–12556.
[34] X. Wua, J. Cai, S. Li, F. Zheng, Z. Lai, L. Zhu, T. Chen, Adv. Colloid Interface Sci. 469 (2016) 138–146.
[35] W. Zhang, B. Wang, C. Hao, Y. Liang, H. Shi, L. Ao, W. Wang, J. Alloy. Comp. 684 (2016) 445–452.
[36] S. Ren, B. Wang, H. Zhang, P. Ding, Q. Wang, ACS Appl. Mater. Interfaces 7 (2015) 4066–4074.
[37] Y. Pan, S. Deng, L. Polavarapu, N. Gao, P. Yuan, C.H. Sow, Q.-H. Xu, Langmuir 28 (2012) 12304–12310.
[38] J. Niu, Y. Dai, L. Yin, J. Shangb, J.C. Crittenden, Phys. Chem. Chem. Phys. 17 (2015) 17421–17428.
[39] N. Meir, I.J.-L. Plante, K. Flomin, E. Chockler, B. Moshofsky, M. Diab, M. Volokh, T. Mokari, J. Mater. Chem. A Mater. Energy Sustain. 1 (2013) 1763–1769.
[40] B. Wang, R. Li, Z. Zhang, W. Zhang, X. Yan, X. Wu, G. Chengac, R. Zheng, J. Mater. Chem. A Mater. Energy Sustain. 5 (2017) 14415–14421.
[41] L. Sinatra, A.P. LaGrow, W. Peng, A.R. Kirmani, A. Amassian, H. Idriss, O.M. Bakr, J. Catal. 322 (2015) 109–117.
[42] Y.-K. Lin, Y.-J. Chiang, Y.-J. Hsu, Sens. Actuator B-Chem. 204 (2014) 190–196.
[43] J. Polte, T.T. Ahner, F. Delissen, S. Sokolov, F. Emmerling, A.F. Thünemann, R. Kraehnert, J. Am. Chem. Soc. 132 (2010) 1296–1301.
[44] Z. Li, Y. Pi, D. Xu, Y. Li, W. Peng, G. Zhang, F. Zhang, X. Fan, Appl. Catal. B Environ. 213 (2017) 1–8.
[45] Y.-H. Chiu, K.-D. Changb, Y.-J. Hsu, J. Mater. Chem. A Mater. Energy Sustain. 6 (2018) 4286–4296.
[46] T.-T. Yang, W.-T. Chen, Y.-J. Hsu, K.-H. Wei, T.-Y. Lin, T.-W. Lin, J. Phys. Chem. C 114 (2010) 11414–11420.
[47] Y.-C. Chen, T.-C. Liu, Y.-J. Hsu, ACS Appl. Mater. Interfaces 7 (2015) 1616–1623.
[48] S. Das, S. Sinha, B. Das, R. Jayabalan, M. Suar, A. Mishra, A.J. Tamhankar, C.S. Lundborg, S.K. Tripathy, Sci. Rep. 7 (2017) 104–117.
[49] Y. Jia, S. Zhan, S. Ma, Q. Zhou, ACS Appl. Mater. Interfaces 8 (2016) 6841–6851.
[50] D. Venieria, A. Fraggedakia, M. Kostadimaa, E. Chatzisymeona, V. Binasb, A. Zachopoulosb, G. Kiriakidisb, D. Mantzavinos, Appl. Catal. B-Environ. 154 (2014) 93–101.
[51] D. Xia, Z. Shen, G. Huang, W. Wang, J.C. Yu, P.K. Wong, Environ. Sci. Technol. 49 (2015) 6264–6273.
[52] H.F. Diao, X.Y. Li, J.D. Guc, H.C. Shi, Z.M. Xie, Process Biochem. 39 (2004) 1421–1426.
[53] W. Yin, J. Yu, F. Lv, L. Yan, L.R. Zheng, Z. Gu, Y. Zhao, ACS Nano 10 (2016) 11000–11011.
[54] A.Y. Booshehri, M.I. Polo-Lopez, M. Castro-Alférez, P. He, R. Xu, W. Rong, S. Malato, P. Fernández-Ibáñez, Catal. Today 281 (2017) 124–134.
[55] K. Ouyang, K. Dai, S.L. Walker, Q. Huang, X. Yin, P. Cai, Sci. Rep. 6 (2016) 25702–25709.
[56] F. Gosselin, L.M. Madeira, T. Juhna, J.C. Block, Water Res. 47 (2013) 5631–5638.
[57] A. Selvakumar, M.E. Tuccillo, S. Muthukrishnan, A.B. Ray, Remed. J. 19 (2009) 135–142.
[58] Yi-Hsuan Chiu, Yung-Jung Hsu, Nano Energy 31 (2017) 286–295.
[59] Y.-C. Pu, H.-Y. Chou, W.-S. Kuo, K.-H. Wei, Y.-J. Hsu, Appl. Catal. B Environ. 204 (2017) 21–32.
[60] J.-L. Guo, Y.-D. Chiou, W.-I. Liang, H.-J. Liu, Y.-J. Chen, W.-C. Kuo, C.-Y. Tsai, K.-An Tsai, H.-H. Kuo, W.-F. Hsieh, J.-Y. Juang, Y.-J. Hsu, H.-J. Lin, C.-T. Chen, X.-P. Liao, B. Shi, Y.-H. Chu, Adv. Mater. 25 (2013) 2040–2044.